The Crystal Structure of Coxsackievirus B3 RNA-Dependent RNA Polymerase in Complex with Its Protein Primer VPg Confirms the Existence of a Second VPg Binding Site on *Picornaviridae* Polymerases[▽]

Arnaud Gruez,[1][†][‡] Barbara Selisko,[1][†]* Michael Roberts,[2] Gérard Bricogne,[2] Cécile Bussetta,[1] Ilham Jabafi,[1] Bruno Coutard,[1] Armando M. De Palma,[3] Johan Neyts,[3] and Bruno Canard[1]*

Architecture et Fonction des Macromolécules Biologiques, CNRS and Universités d'Aix-Marseille I et II, UMR 6098, ESIL Case 925, 13288 Marseille, France[1]; Global Phasing, Ltd., Sheraton House, Castle Park, Cambridge CB3 0AX, United Kingdom[2]; and Rega Institute for Medical Research, Katholieke Universiteit Leuven, Leuven, Belgium[3]

The RNA-dependent RNA polymerase (RdRp) is a central piece in the replication machinery of RNA viruses. In picornaviruses this essential RdRp activity also uridylates the VPg peptide, which then serves as a primer for RNA synthesis. Previous genetic, binding, and biochemical data have identified a VPg binding site on poliovirus RdRp and have shown that is was implicated in VPg uridylation. More recent structural studies have identified a topologically distinct site on the closely related foot-and-mouth disease virus RdRp supposed to be the actual VPg-primer-binding site. Here, we report the crystal structure at 2.5-Å resolution of active coxsackievirus B3 RdRp (also named 3D^{pol}) in a complex with VPg and a pyrophosphate. The pyrophosphate is situated in the active-site cavity, occupying a putative binding site either for the coproduct of the reaction or an incoming NTP. VPg is bound at the base of the thumb subdomain, providing first structural evidence for the VPg binding site previously identified by genetic and biochemical methods. The binding mode of VPg to CVB3 3D^{pol} at this site excludes its uridylation by the carrier 3D^{pol}. We suggest that VPg at this position is either uridylated by another 3D^{pol} molecule or that it plays a stabilizing role within the uridylation complex. The CVB3 3D^{pol}/VPg complex structure is expected to contribute to the understanding of the multicomponent VPg-uridylation complex essential for the initiation of genome replication of picornaviruses.

Picornaviridae form a large virus family, which comprises important human and animal pathogens, such as poliovirus (PV), coxsackieviruses, rhinoviruses, hepatitis A virus, and foot-and-mouth disease virus (FMDV). Coxsackieviruses belong to the *Enterovirus* genus (68). Infections caused by coxsackievirus B serotype 3 (CVB3) are at the origin of 20 to 30% of all human cases of acute and chronic myocarditis (19). Furthermore, CVB3 causes acute infections in neonates and infants leading to febrile illness and meningitis, as well as hepatitis and coagulopathy in severe cases (71). To date, no vaccine or specific anticoxsackievirus drug is approved (2, 60).

Unlike many other positive-strand RNA viruses, the genome of *Picornaviridae* is not capped at the 5′ end but decorated with a covalently linked 22-amino-acid peptide named VPg (for virion protein genome-linked). Translation is thus cap independent, and ribosomes use an internal ribosome entry site situated in the 5′ untranslated region of the polyadenylated VPg-RNA. A single open reading frame in the genomic positive-strand RNA encodes a polyprotein of around 250 kDa consisting of one structural region (P1) and two nonstructural regions (P2 and P3). The information on *Enterovirus* polyprotein processing and RNA replication is essentially based on the prototypic PV. Currently, a general consensus exists that the mechanism of PV RNA replication is applicable to coxsackieviruses (59). Viral proteases 2A^{pro}, 3C^{pro}, and 3CD^{pro} process the polyprotein in a highly regulated cascade resulting in a variety of precursor and mature proteins (50). Possibly, all of the nonstructural proteins and their precursors form the membrane-associated replication complex, in which the positive-strand RNA genome serves as a template for negative-strand RNA synthesis, which is then transcribed into positive-strand RNA. The most important and stable cleavage products of P3 are proteins 3AB and 3CD^{pro}. Cleavage of protein 3AB yields the membrane-anchor 3A, and VPg (or 3B) of 22 amino acids. The 3CD^{pro} precursor cleavage leads to 3C^{pro} and 3D^{pol}, the latter being the viral RNA-dependent RNA polymerase (RdRp).

The RdRp of RNA viruses plays an essential role in viral replication. It has no equivalent in the host cell thus far and represents a prime target for the development of antiviral drugs. Currently, three-dimensional structures of RdRps (or RdRp domains) have been determined for 10 positive-strand RNA viruses from the *Picornaviridae*, *Caliciviridae*, and *Flaviviridae* families and for three double-stranded RNA viruses from the *Reoviridae*, *Birnaviridae*, and *Cystoviridae* families

* Corresponding authors. Mailing address: Architecture et Fonction des Macromolécules Biologiques, CNRS and Universités d'Aix-Marseille I et II, UMR 6098, ESIL Case 925, 13288 Marseille, France. Phone: 33 491 82 86 44. Fax: 33 491 82 86 46. E-mail address for B. Selisko: barbara.selisko@afmb.univ-mrs.fr. E-mail address for B. Canard: bruno.canard@afmb.univ-mrs.fr.

† A.G. and B.S. contributed equally to this study.

‡ Present address: Laboratoire de Maturation des ARN et Enzymologie Moléculaire, UMR, 7567, Université Henri Poincaré Nancy I, Vandoeuvre-les-Nancy, France.

▽ Published ahead of print on 16 July 2008.

(nine structures are reviewed in reference 13; see also references 17, 35, 43, and 70). Although they share little sequence identity, they all adopt a similar canonical fold resembling a cupped right hand with fingers, palm, and thumb subdomains. Nevertheless, structural elements important for binding a potential drug may vary significantly between RdRps of the same viral family and even the same genus. The structurally most conserved RdRp subdomain is the catalytic palm subdomain where, as in most other polymerases (8, 62), two catalytic aspartic acid side chains coordinate two divalent metal ions essential for catalysis. The fingers and thumb subdomains are involved in template, primer, and NTP substrate binding. The conformation of the thumb subdomain is related to the mode of initiation of the RdRp being either primer dependent or primer independent (de novo) (13). In vitro most of the RdRps are able to support both, and recent results indicate that some may do so in vivo (55, 56). Fingers and thumb subdomains are in contact with each other, thus the RdRps' active site is encircled and sits in the center, to which the substrates have access through channels or tunnels. During RNA synthesis RdRps seem to undergo rather small conformational changes (13, 14). This is in contrast to large subdomain movements causing the closure of a rather open right-hand structure of other polymerases (DNA-dependent DNA or RNA polymerases and reverse transcriptases) over the primer-template (10).

Picornaviridae RdRps use VPg as a primer for positive-strand and negative-strand RNA synthesis. VPg is uridylated by 3D^{pol}, which covalently links two UMPs to VPg residue Tyr3. For enteroviruses this reaction is templated either by a *cis*-acting replication element (*cre*), a stem-loop situated in the coding region of protein 2C [*cre*(2C)], or the poly(rA) tail, albeit with lower efficiency in vitro (48). 3D^{pol} uses the same mechanism and the same active site for VPg-uridylation as for processive RNA synthesis, as demonstrated by the sensitivity of the VPg-uridylation reaction to mutations of the two catalytic aspartic acids in the 3D^{pol} active site (34). For PV it was shown that *cre*(2C)-templated VPg-uridylation was important for the initiation of positive-strand RNA synthesis, whereas it seemed not to be required for negative-strand RNA synthesis (20, 37, 38). The poly(rA) tail was proposed to act as the template for the initiation of negative-strand RNA synthesis in vivo (38, 48). In contrast, CVB3 *cre*(2C) seems to be involved in the initiation of both positive-strand and negative-strand RNA synthesis (67). According to current models, CVB3 RNA genome replication might proceed as follows: 3AB acts as a membrane-anchor of mature 3D^{pol}. Some evidence has been presented that active 3D^{pol} forms oligomeric structures (25, 45). Dimeric 3CD^{pro} binds and delivers template *cre*(2C). The formation and stability of the replication complex is mediated by a direct interaction between 3D^{pol} and 3C (44). Uridylation of VPg takes place in this complex. It is still not clear whether VPg is liberated from 3AB by 3CD^{pro} before or after uridylation (16, 31). The initiation complex may then dissociate from *cre*(2C). It is not clear whether VPg-pUpU stays bound to 3D^{pol} (9, 38, 69). CVB3 VPg-pUpU is expected to base-pair to the poly-adenylated 3′ end of positive-strand RNA and thus prime negative-strand RNA synthesis for 3D^{pol} (67). Alternatively, PV negative-strand RNA synthesis may start by uridylation of VPg using directly poly(rA) as an initiation and elongation

template (38). For both viruses, VPg uridylation on *cre*(2C) precedes positive-strand RNA synthesis where VPg-pUpU base-pairs to two adenosines at the 3′ end of newly synthesized (−) RNA (24).

VPg residue Tyr3 is strictly conserved throughout the *Picornaviridae* family. *Enterovirus* VPgs show an overall sequence conservation of ca. 75%. The comparison of *Enterovirus* VPgs to VPgs of other genera shows ca. 35% sequence identity with *Rhinovirus* VPgs and ca. 15% sequence identity with *Aphthovirus* (prototype FMDV), *Hepatovirus*, and *Cardiovirus* VPgs. The nuclear magnetic resonance structure of PV VPg in solution has shown that it is intrinsically flexible in low-salt buffer (58). A major conformational change was observed in a stabilizing solution, perhaps mimicking induced folding upon binding to 3D^{pol} (58). Concerning the VPg-binding site on 3D^{pol}, two different sites seem to coexist. The first complete crystal structures of *Picornaviridae* RdRps of various human rhinovirus (HRV) strains (1, 32) showed a widely open access to the active site from the "front" of the RdRp. Accordingly, a model was proposed that accommodated the VPg primer in a "front-loading" position (1). This was indeed demonstrated by the crystal structure of the FMDV RdRp in complex with VPg-pU (12). Another VPg binding site had been mapped earlier by several series of elegant genetic and biochemical experiments (26, 34, 64). These studies converged to a series of amino acids located around Val391 at the "back" of PV 3D^{pol} near the base of the thumb subdomain. The two VPg binding modes cannot be reconciled into a VPg uridylation scheme involving a single 3D^{pol} molecule, at least without dissociation and reassociation of VPg-pUpU. A model of the PV 3D^{pol} in complex with VPg occupying the second binding site (64) proposes that residue Tyr3 of VPg enters the active site from the back via the NTP-entry tunnel. This corresponds to the finding that 3D^{pol} residues situated at the entrance of the NTP-entry tunnel are important for VPg-uridylation but not for RNA synthesis (34). VPg-pUpU elongation would then be completed after its dissociation and reassociation to 3D^{pol}, this time entering from the front.

Here we present the three-dimensional structure, obtained by X-ray crystallography, of coxsackievirus B3 (CVB3) RdRp, also named 3D^{pol}. The recombinant protein is active in vitro for both VPg-uridylation and RNA elongation. We also report the crystal structure of the complex of 3D^{pol} with its viral protein primer VPg and a pyrophosphate (PP$_i$). The PP$_i$ is situated in the active site cavity, occupying a putative binding site either for the coproduct of the reaction or an incoming NTP. VPg is bound at the base of the thumb subdomain, thus providing the first structural support for the second binding site for VPg for which genetic and biochemical evidence had previously emerged (26, 34, 64).

MATERIALS AND METHODS

A synthetic, high-pressure liquid chromatography-purified CVB3 VPg peptide (GAYTGVPNQKPRVPTLRQAKVQ) was purchased from Synprosis (Marseille, France). The peptide was solubilized in 10 mM Tris (pH 7.5)–25 mM NaCl–10% glycerol and stored at −20°C.

RdRp activity tests. CVB3 3D^{pol} (strain Nancy, GenBank accession no. gi: 323421), bearing a His$_6$ tag at the C-terminal end, was expressed and purified as described in reference 27. Filter-binding RdRp activity assays were conducted in 40 μl of 50 mM HEPES (pH 8.0) (or 50 mM Tris [pH 8.0]) and 10 mM KCl containing 400 nM poly(rA) (GE Healthcare; average size, 357 nucleotides)

annealed to 10 μM dT$_{15}$ (Invitrogen), 400 nM CVB3 3D^{pol}, 9% glycerol, MgCl$_2$ or MnCl$_2$ at the concentrations given in Fig. 2A, 10 μM UTP, and 0.4 μCi of [^{3}H]UTP (GE Healthcare; 12 Ci/mmol). Reactions were started with a premix of MgCl$_2$ (or MnCl$_2$) and UTP and incubated at 30°C. Samples of 12 μl were taken after 5 and 30 min and added to 30 μl of 50 mM EDTA in 96-well sample plates. Stopped reaction samples were then transferred onto glass fiber filter mats with DEAE active groups (DEAE Filtermat; Wallac) using a Filtermat Harvester (Packard Instruments). Filtermats were washed three times with 0.3 M ammonium formate (pH 8.0), twice with water, and once with ethanol; dried; and transferred into sample bags. Liquid scintillation fluid was added, and incorporation was measured in counts per minute by using a Wallac MicroBeta TriLux liquid scintillation counter.

Gel-based RdRp activity assays made use of ^{32}P-labeled UTP, and reactions were monitored by using denaturing polyacrylamide gel electrophoresis (PAGE). Poly(rA)/dT$_{15}$ was used as a template-primer system [or poly(rA) alone when indicated] following the same protocol as given above except that 0.8 mM MgCl$_2$, 1 μM CVB3 RdRp, and 4 μCi of [α-^{32}P]UTP (GE Healthcare; 6,000 Ci/mmol) were used. Samples were taken after 5, 10, and 30 min, and reactions were quenched by adding formamide-EDTA gel loading buffer. Reaction products were separated by using electrophoresis on a 14% acrylamide-bisacrylamide (19:1) gel containing 7 M urea using TTE buffer (89 mM Tris [pH 8.0] 28 mM taurine [2-aminoethanesulfonic acid], 0.5 mM EDTA). RNA product bands were visualized by using photostimulated plates and a fluorescent image analyzer FLA3000 (Fuji). Markers were prepared by labeling dT$_{15}$ and poly(rA) with T4 polynucleotide kinase (T4 PNK; Biolabs) and [γ-^{32}P]ATP (GE Healthcare).

The VPg uridylation assay in the presence of poly(rA) was done using the reaction conditions given above, with the following concentration adjustments: 2 μM CVB3 RdRp, 200 μM CVB3 VPg, 400 nM poly(rA), 0.8 mM MgCl$_2$, or 0.1 mM MnCl$_2$. Samples were taken after 1 and 2 h, and each aliquot was mixed with the same volume of 2× Tris-Tricine sodium dodecyl sulfate (SDS) sample buffer (100 mM Tris [pH 6.8], 19% [vol/vol] glycerol, 8% SDS, 4% β-mercaptoethanol, bromophenol blue). Reaction products were separated by using Tris-Tricine SDS-PAGE in a 4% stacking gel (acrylamide-bisacrylamide [37.5:1], 750 mM Tris [pH 8.45], 0.075% SDS), 10% spacer gel (acrylamide-bisacrylamide [29:1], 1 M Tris [pH 8.45], 0.1% SDS), and 15% separating gel (acrylamide-bisacrylamide [29:1], 1 M Tris [pH 8.45], 0.1% SDS). Running buffers contained 0.2 M Tris (pH 8.9) as anode buffer and 0.1 M Tris, 0.1 M Tricine (pH 8.25), and 0.1% SDS as cathode buffer. Product bands were visualized as detailed above.

Crystallization, data collection, and processing. CVB3 3D^{pol} was crystallized using the crystallization conditions as described in reference 27. The CVB3 3D^{pol}/VPg complex was obtained by preparing a mix of 220 μM CVB3 3D^{pol} (in 20 mM Tris [pH 9.0], 300 mM NaCl, 15% glycerol, 0.5 mM Tris(2-carboxyethyl) phosphine), 440 μM VPg (in 10 mM Tris [pH 7.5], 25 mM NaCl, and 10% glycerol), 1 mM oligoA$_6$, 2.5 mM 3′dUTP, and 10 mM MgCl$_2$. The mix was incubated for 24 h on ice prior to crystallization using two parts 2.0 M (NH$_4$)$_2$SO$_4$–100 mM CAPS (pH 10)–200 mM Li$_2$SO$_4$ and one part 1.3 to 1.8 M NH$_4$Cl–100 mM sodium acetate (pH 4.6 to 5.2) by volume (27). Tetragonal crystals (P4$_3$2$_1$2, a = b = 74.38 Å, c = 285.81 Å) appeared 3 weeks after mixing the sample solution with the well buffer at a ratio of 4.3 to 3.7 (vol/vol). Crystals were flash-frozen in the crystallization solution supplemented with 28% glycerol. Cocrystallization of CVB3^{pol} with ligands (3′dUTP, UTP, CTP, ATP, or GTP, as well as magnesium or manganese ions) was also attempted. CVB3^{pol}/NTP complexes were obtained by mixing 220 μM CVB3 3D^{pol} with 10 mM NTP and 10 mM MgCl$_2$ or MnCl$_2$. The protein-ligand solutions were kept on ice for 24 h and crystallized under the same conditions as described above. Crystals were flash frozen in a solution containing 28% glycerol. The crystals belong to the same P4$_3$2$_1$2 space group and have the same unit cell as the ones of the VPg complex. The diffraction data sets were collected on beam line ID14-3 of the European Synchrotron Radiation Facility (ESRF; Grenoble, France) using a MAR 165 charge-coupled device detector. While most of the crystals obtained by cocrystallization with NTPs and ions diffracted to ~3-Å resolution, a data set to a resolution of 2.1 Å was collected for one crystal from the cocrystallization experiment with GTP and MgCl$_2$ (Table 1). It was not possible to collect a more complete data set to even higher resolution because the c unit cell parameter of 285.88 Å did not allow appropriate spot separation at a closer crystal-to-detector distance. For the 3D^{pol}/VPg complex, one data set was collected to 2.5-Å resolution (Table 1). All X-ray data were indexed, integrated, and scaled by using the XDS package (28).

Structure determination and refinement. The structure of the CVB3 3D^{pol}/GTP complex was solved by molecular replacement using the program AMoRe (40) and the crystal structure of PV 3D^{pol} as a model (PDBID 1RA6) (66). The structure was obtained by several rounds of manual building using Turbo-Frodo

(57) and refinement using Refmac5 (39). Water molecules were added by using ARP/warp (49).

The structure of the CVB3 3D^{pol}/3′dUTP/VPg complex was determined by using the previously refined CVB3 3D^{pol}/GTP structure. The initial 2|Fo|-|Fc| and |Fo|-|Fc| residual maps revealed an elongated extra density at the protein surface located between the palm and the thumb subdomains that was interpreted as the bound VPg peptide. Several rounds of building and refinement were performed by using Refmac5. The 2|Fo|-|Fc| maps were weak and the |Fo|-|Fc| residual maps during the refinement were noisy when building the VPg at its binding site, precluding any side chain identification. Subsequently, the crystal structure was rerefined by using Buster-TNT 2.1.1. (3). The quality of the 2|Fo|-|Fc| and |Fo|-|Fc| residual maps was clearly improved, making it possible to build the VPg molecule and to refine the structure through several rounds of alternate building and refinement using the Coot (11) and BUSTER-TNT programs. In order to compare the structures of both complexes, the CVB3 3D^{pol}/GTP structure was also rerefined using the BUSTER-TNT program. The final rounds of refinement of the VPg complex were performed by invoking a recent enhancement of the BUSTER-TNT program, namely, the use of local structure similarity restraints (LSSR) (61). Interatomic distances within the structure being refined are restrained to remain similar to those occurring in an external "target" structure to which it is believed to be closely similar. The LSSR functional form is not harmonic, but plateaus for large differences of interatomic distances, thus automatically allowing departures from the target structure to be accommodated if the X-ray data so demand. Here, the 3D^{pol} domain of the 3D^{pol}/3′dUTP/VPg complex was targeted to the higher-resolution structure of the 3D^{pol}/GTP complex, thus preventing it from "unrefining" against the lower-resolution data. Refinement statistics of both complexes are summarized in Table 1.

Protein structure accession numbers. The protein structure coordinates of CVB3 3D^{pol} structures in complex with GTP, as well as with VPg and 3′dUTP, have been deposited at the Protein Data Bank under accession numbers 3CDU and 3CDW, respectively.

RESULTS

In vitro primer-dependent RNA synthesis and VPg uridylation by CVB3 RdRp. Recombinant CVB3 3D^{pol} showed primer-dependent RNA synthesis activity using poly(rA)/(dT)$_{15}$ as a template-primer system, in Mn^{2+}- and Mn^{2+}-containing buffers. Optimum ion concentrations were determined for both (Fig. 1A), yielding 0.8 and 0.1 mM as the optimum concentrations of Mg^{2+} and Mn^{2+}, respectively. CVB3 RdRp was twice as active at the Mn^{2+} concentration optimum compared to that of Mg^{2+}. Primer dependency and usage at the optimal Mg^{2+} concentration was visualized by PAGE, as illustrated in Fig. 1B. A poly(U) polymerization product is only observed when oligo(dT)$_{15}$ is present. Products are longer than (dT)$_{15}$ (lane T), suggesting that the primer is enlongated, generating oligo(dT)$_{15}$-poly(U) products. A ladder of products is generated, which corresponds to the variation in size of the homopolymeric template (lane A). VPg uridylation was tested using poly(rA) as a template at optimum concentrations of either Mg^{2+} or Mn^{2+}, and reaction products were visualized by using Tris-Tricine PAGE (Fig. 1C). Only in the presence of Mn^{2+}, poly(rA), and VPg, did CVB3 3D^{pol} generate two bands. The faster-migrating double-band can be attributed to VPg-pU(pU) (4, 48, 53). The slower-migrating band might correspond to VPg-poly(U) produced by primer elongation on poly(rA), 3D^{pol}-pU(pU), which has been shown to be generated by intra- or intermolecular uridylation of PV 3D^{pol} (53), or to poly(rA)-(pU)$_n$ generated by a terminal transferase activity of 3D^{pol} (4, 41).

The three-dimensional structures of CVB3 RdRp complexes. The best-diffracting NTP-3D^{pol} crystals were obtained from a cocrystallization mix containing CVB3 3D^{pol} with GTP and Mg^{2+}. The structure (resolution, 2.1 Å) was solved by

TABLE 1. Data collection and refinement statistics

Parameter[a]	Complex[b]	
	3D^{pol}/GTP(PP$_i$)	3D^{pol}/3′dUTP(PP$_i$)/VPg
X-ray source	ID14-3, ESRF	ID14-3, ESRF
Wavelength (Å)	0.9330	0.9330
Space group	P4$_3$2$_1$2	P4$_3$2$_1$2
Crystal parameters (Å)	a = b = 74.40, c = 285.88	a = b = 74.21, c = 285.59
Resolution (Å)	74.3–2.1 (2.23–2.10)	27.45–2.5 (2.64–2.50)
No. of unique data	40,919	28,791
No. of observations	196,486	185,836
Redundancy	4.80 (2.0)	6.45 (4.0)
Completeness (%)	90.6 (52.6)	99.9 (99.7)
Mean $I/\sigma I$	25.4 (6.2)	17.0 (2.6)
R$_{sym}$ (%)	3.8 (9.3)	8.4 (38.6)
Refinement using BUSTER-TNT		
Resolution range (Å)	71.98–2.10	27.45–2.50
Last shell range (Å)	2.23–2.10	2.65–2.50
No. of reflections (working set)	38,755	27,251
No. of reflections (test set)	2,057	1,451
R$_{work}$ (overall)	0.1776	0.1757
R$_{work}$ (last shell)	0.1905	0.2071
R$_{free}$ (overall)	0.2196	0.2174
R$_{free}$ (last shell)	0.2303	0.2571
No. of amino acid residues	468	477
RMSD from ideal geometry		
Covalent bond length (Å)	0.010	0.008
Bond angle (°)	1.157	1.046
ESD from Luzzati plot (Å)	0.2248	0.2710
Avg B factor (main chain) (Å^2)	26.8	41.2 (VPg, 75.5)
Avg B factor (side chain) (Å^2)	33.1	47.4 (VPg, 83.3)
Ramachandran plot analysis (from Molprobity)		
Residues in favored regions (%)	98.71	98.73
Outliers (%)	0.00	0.00

[a] $R_{sym} = \Sigma_h\Sigma_j|I_{h,j} - \langle I_h\rangle|/\Sigma_h\Sigma_j I_{h,j}$, where I denotes an intensity, h is a triple of Miller indices for a symmetry-unique reflection measured more than once, j indexes the independent measurements of reflections equivalent to a given symmetry-unique reflection, and $\langle I_h\rangle$ is the average of the $I_{h,j}$ over the various values of j; $R = \Sigma_h||F_{obs}| - \langle|F_{calc}|\rangle|/\Sigma_h|F_{obs}|$, where $\langle|F_{calc}|\rangle$ is the expectation of $|F_{calc}|$ under the error model used in maximum-likelihood refinement, R_{work} is the value of R calculated over the working set, and R_{free} is the value of R calculated over the test set; ESD, estimated standard deviation.
[b] The Protein Data Bank accession numbers for complexes 3D^{pol}/GTP(PP$_i$) and 3D^{pol}/3′dUTP(PP$_i$)/VPg are 3CDU and 3CDW, respectively.

molecular replacement using the structure of PV RdRp as a search model. The complex structure with VPg (resolution, 2.5 Å) was obtained using crystals grown in a mix of VPg, an oligo(rA)$_6$ template, 3′dUTP, and Mg^{2+}. The statistics of the refinements using BUSTER-TNT (see Materials and Methods) are summarized in Table 1. Both refined structures contain the complete protein (462 residues plus the six C-terminal histidines of the His$_6$ tag) and six acetate ions. In addition, the 3D^{pol}/GTP structure contains six chloride ions, one sulfate ion, and 30 glycerol and 321 water molecules. The 3D^{pol}/3′dUTP/VPg complex contains 7 chloride ions and 27 glycerol and 318 water molecules. No metal ion is present in the structures, but a PP$_i$ is seen in both structures near the active site (see below). In the 3D^{pol}/3′dUTP/VPg complex, additional density clearly indicates the presence of the 7-PNQKPRVPT-15 peptide of CVB3 VPg at the back of the molecule at the base of the thumb subdomain (see below). The root mean square deviation (RMSD) between both structures is extremely low (0.089 Å after superimposition of the C$_\alpha$ atoms of 468 amino acids), indicating that no rearrangement of the 3D^{pol} structure was needed during refinement to account for the X-ray data from the complex obtained after VPg binding. There is, however, one localized difference: the side chain of Glu383 is switched so as to H-bond with Gln9 of VPg. These observations are consistent with the property of LSSR used during refinement

(see Materials and Methods). They favor retention of overall structure, while allowing localized changes demanded by the X-ray data, i.e., by difference maps.

Overall three-dimensional structure of CVB3 RdRp. CVB3 RdRp adopts the canonical right-hand architecture of RdRps with the N- and C-terminal fingers and thumb subdomains interacting to encircle the active site. Figure 2A shows the structural superimposition of CVB3 RdRp with PV RdRp (73.1% sequence identity) used as a template for molecular replacement. The protein structure comparison service SSM (29) yielded an RMSD of 0.7 Å for 460 superposed residues. RMSDs to HRV14 RdRp (66.0% sequence identity, see also alignment in Fig. 3) and FMDV RdRp (30.0% sequence identity) of *Picornaviridae* were found to be 1.0 Å (453 superposed residues) and 1.7 Å (433 residues), respectively. The structural comparison with RdRp structures of other viral families of positive-strand RNA viruses gave RMSDs of 2.1 Å (407 residues) to rabbit hemorrhagic disease virus (*Caliciviridae*, 22.4% sequence identity) RdRp (42) and 3.0 Å (354 residues) to hepatitis C virus (HCV; *Flaviviridae*, 9.3% sequence identity) RdRp (5).

The classic subdomains are shown in Fig. 2A delineated as fingers (amino acids 1 to 69, 96 to 190, and 271 to 285), palm (amino acids 70 to 95, 191 to 270, and 286 to 380), and thumb (amino acids 381 to 462). Motifs A to F (6) and G, the latter
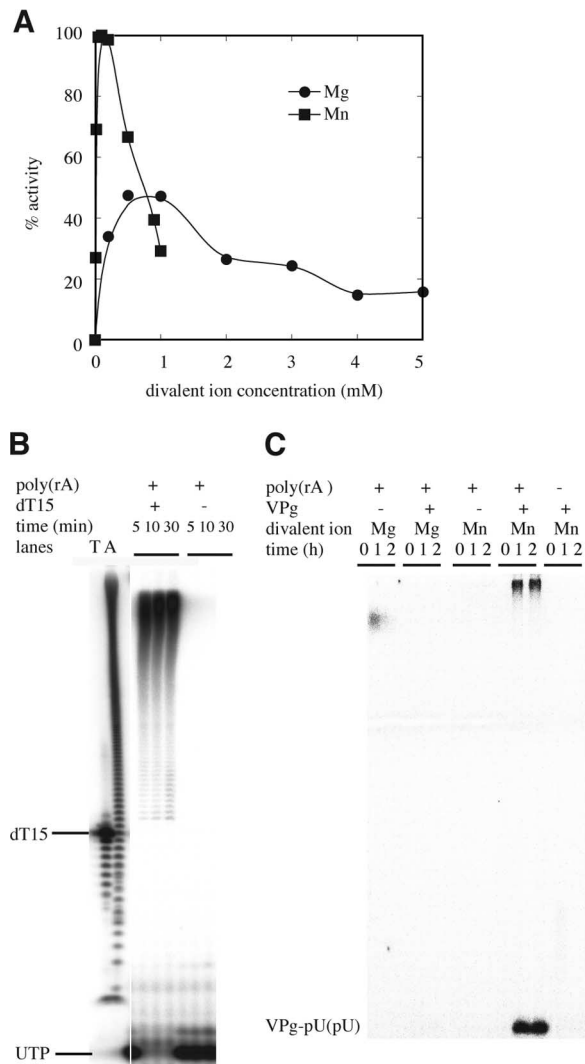
FIG. 1. Primer-dependent activity of CVB3 RdRp. (A) Divalent ion optima for primer-dependent RdRp reaction using poly(rA)/(dT)$_{15}$ as determined by filter-binding assay (see Material and Methods). The optimum values for MgCl$_2$ and MnCl$_2$ were found to be 0.8 and 0.1 mM, respectively. Maximum activity (counts per minute after 30 min) obtained at the optimum of MnCl$_2$ was set to 100%. (B) Time course of primer-dependent (dT)$_{15}$-poly(U) synthesis using primer/template poly(rA)/(dT)$_{15}$. Reactions were conducted in the presence of 0.8 mM MgCl$_2$ and analyzed by denaturing PAGE. No RdRp activity was detectable in the absence of primer dT$_{15}$. Lane T corresponds to ^{32}P-labeled (dT)$_{15}$, and lane A corresponds to ^{32}P-labeled template poly(rA). (C) VPg uridylation by CVB3 3D^{pol} in the presence of poly(rA), synthetic CVB3 VPg, and 0.1 mM MnCl$_2$. Samples were taken after 1 and 2 h and analyzed by using Tris-Tricine-SDS-PAGE.
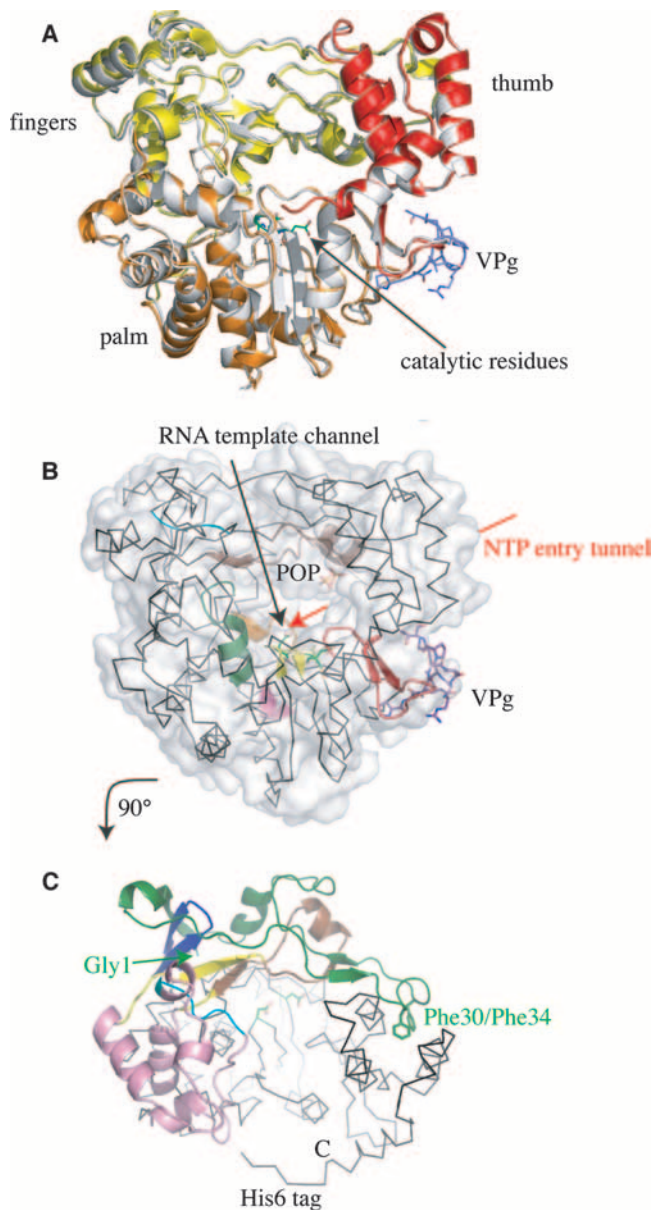

FIG. 2. Structure of CVB3 RdRp. (A) Front view of CVB3 RdRp with the subdomains colored in yellow (fingers), orange (palm), and red (thumb). VPg is shown in sticks bound to the base of the thumb. CVB3 is superimposed onto PV RdRp (PDB ID: 1RA6) used for molecular replacement (white). The catalytic residues Asp233 and Asp326 in the active site cavity are shown in sticks. (B) Space-filled representation of CBV3 RdRp indicating the RNA template channel and the NTP entry tunnel at the back of the molecule and showing RdRp motifs A (orange), B (green), C (yellow), D (pink), E (red), F (brown), and G (cyan). (C) Top view of CVB3 RdRp looking down the template channel toward the active-site residues indicated in sticks. The fingers subdomain consists of the index finger (green), middle finger (purple), ring finger (yellow with motif F in brown), and pinky finger (in pink with motif G in cyan). The C terminus of the protein is indicated, as is the His$_6$ tag, which reaches over the front of the molecule from the thumb to the palm subdomain. Structure representations in this and other figures were prepared with PyMOL.
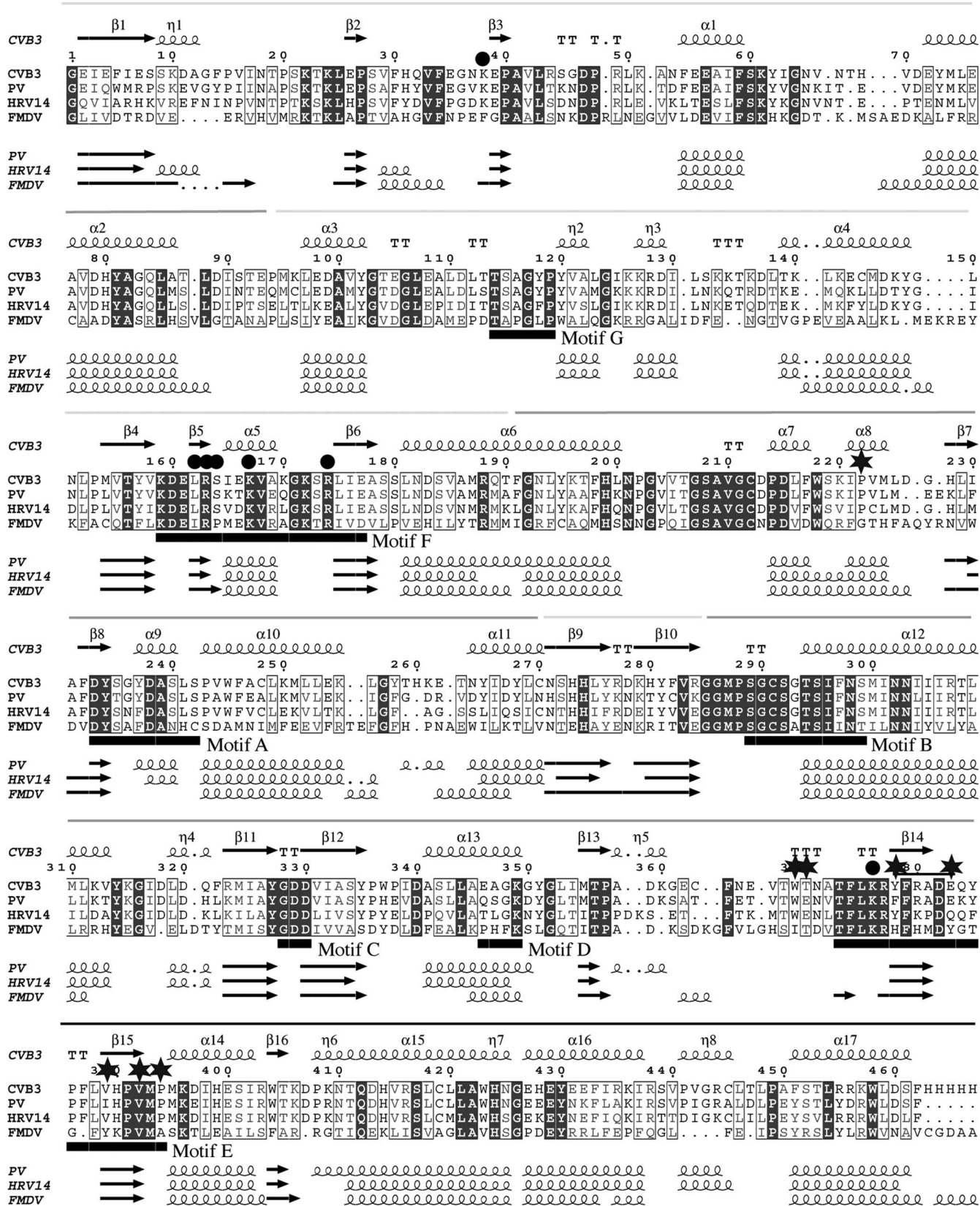
having been proposed as a sequence signature for primer-dependent RdRps (21), are shown in Fig. 2B and 3. Figure 2B also illustrates the RNA template entry channel, as seen in the structure of FMDV RdRp in complex with a primer-template complex (15) and the NTP entry tunnel. The fingers subdomain can be divided into individual fingers according to the convention adopted for PV RdRp (66). The index finger (amino acids 1 to 69, see Fig. 2C) contains a β-strand at the N terminus, which forms the first strand of a five-stranded

FIG. 3. Structural sequence alignment of RdRps of CVB3, PV, HRV14, and FMDV. CVB3 3D^{pol} (genus *Enterovirus*) was aligned to three *Picornaviridae* RdRps with known structures: PV RdRp (genus *Enterovirus*, PDB ID:1RA7) (66), HRV14 (genus *Rhinovirus*, PDB ID:1XR5) (32), and FMDV (genus *Aphtovirus*, PDB ID:2F8E) (12). Secondary structural elements are given for CVB3 RdRp above and for the rest below the sequences. Subdomains are indicated as horizontal lines above the alignment (fingers in light grey, palm in grey, and thumb in black). Catalytic motifs are indicated as horizontal bars. Residues in CVB3 RdRp, which contact the PP$_i$ and VPg, are marked by green or blue stars, respectively. The alignment was done by using the protein structure comparison service SSM at the European Bioinformatics Institute (29), and the figure was made by using Espript (22).

9582

β-sheet. As reported for PV RdRp (66), the very first residue, Gly1, is anchored to residues of the "root" of the index finger (Gly64 and Asn65) and of the palm domain near catalytic motif A (Ala239 and Leu241). These residues are conserved between CVB3 and PV RdRps. The index finger provides the upper part of the RNA entry channel and the tight connection between fingers and thumb subdomain. The main anchor is the insertion of Phe30 and Phe34 into the three-helix bundle α14 to α16 of the thumb (Fig. 2C). The middle finger (amino acids 271 to 285) consists of a short β-hairpin at the top of the finger subdomain underneath the base of the index finger. The ring finger (amino acids 150 to 179) provides the lower part of the RNA entry channel and the roof of the NTP entry channel, including the RdRp motif F implicated in NTP-binding (see below). At the tip of the ring finger residue Leu162 is situated in a hydrophobic zone that involves residues from thumb helix α14, another link between fingers and thumb. Finally, the pinky finger (amino acids 96 to 149 and amino acids 180 to 190) forms the front side of the fingers and contains motif G at the entrance of the template channel. The palm is the structurally most conserved subdomain among RdRps. It is organized around an antiparallel β-sheet (in CBV3 RdRp β7, β11, and β12, see Fig. 3) flanked on one side by one helix (α8), which interacts with the thumb, and on the other side by eight helices (α2, α3,η2, α4, α6, α10, α12, and α13). The palm subdomain contains motif A with the catalytic residue Asp233, motif B involved in the specific selection of rNTPs as substrates, and the strongly conserved GDD-motif C with catalytic residue Asp329 within the β turn between β11 and β12. The transition between palm and thumb subdomain is provided by structural motif E, which is formed by two antiparallel β-strands (β14 and β15). The short thumb subdomain, typical for primer-dependent RdRps, is predominantly shaped by a three-helix bundle (α14, α15, and α16). The end of the C-terminal helix α17 is anchored to the palm subdomain via a hydrophobic interactions between Phe462, Leu216 of helix α7, and Leu388 in the turn of motif E. Thus, the C terminus is placed near the front-loading primer binding zone and the exit channel of VPg-primed double-stranded RNA (as shown previously [15]). The C-terminal His_6 tag reaches over to the palm-subdomain helix α6 (Fig. 2C).

NTP entry tunnel. The NTP entry tunnel is accessed from the back of the molecule (Fig. 2B). The palm subdomain, namely, the region after motif D, provides the floor of the tunnel. Despite some sequence conservation, this region is variable in terms of structure, especially the stretch around conserved CVB3 $3D^{pol}$ residues Asp359 and Lys360 (Fig. 3). In CVB3 RdRp it forms a small helix (η5), and Lys360 contacts Lys167 situated within motif F at the roof of the NTP entry tunnel via a glycerol molecule (Fig. 4A). Likewise, in the structure of apo-PV RdRp, as well as in the NTP-complex structures characterized thus far (23, 65, 66), the corresponding Lys359 lies in the entrance to the NTP tunnel. In some structures (i.e., Protein Data Base [PDB] ID:2ILZ) it contacts Lys167 via a water molecule (Fig. 4B). In FMDV and HRV14 RdRps the corresponding Lys residue is situated in a loop on the right side of the NTP tunnel entry (not shown), which is consequently wider.

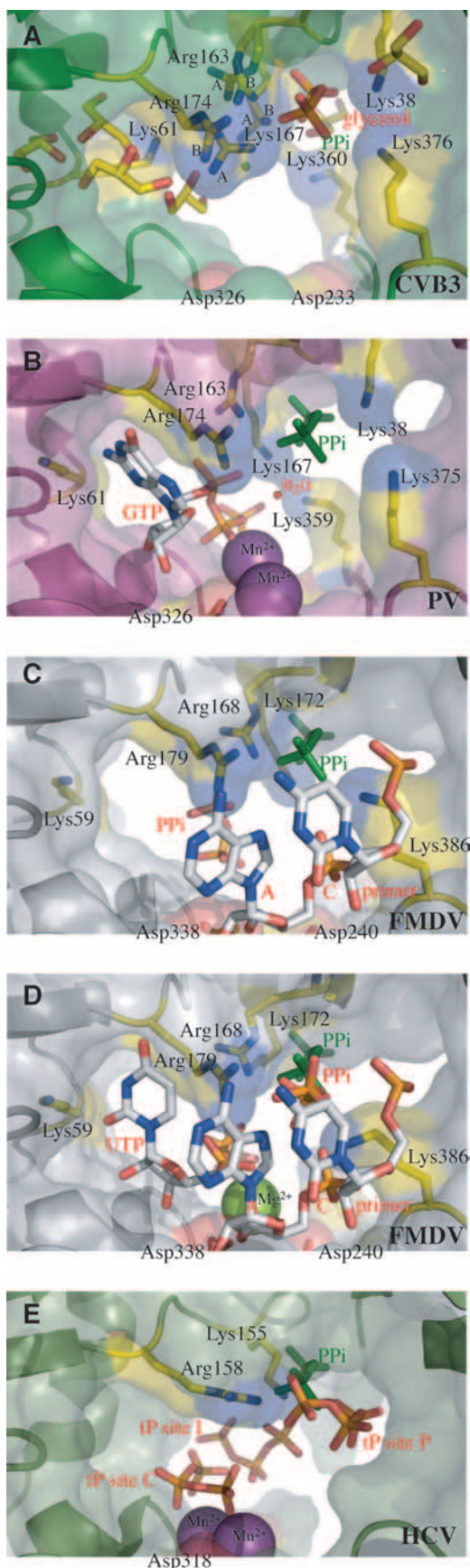A special feature of the CVB3 RdRp structure is the obstruction of the NTP tunnel at the left side by the Lys61 side chain, where in PV RdRp Lys61 is engaged in a salt bridge with Glu177 in the ring finger, forming the tunnel wall (compare Fig. 4A to 4B). This inner salt bridge is conserved in HRV14 RdRp (PDB ID:1XR5) but not in FMDV RdRp, where the distance to the corresponding residue Asp180 in all existing structures (PDB ID:2E9T, 2F8E, 2ECO, 2E9Z, and 2E9R) lies between 4.1 and 8.0 Å. Nevertheless, the corresponding Lys59 in FMDV forms the wall of the NTP-binding cavity (Fig. 4C). In the CVB3 $3D^{pol}$ structure no salt bridge to Glu177 is formed and a glycerol molecule occupies the position of side chain Lys61 adopted in the other *Picornaviridae* RdRps.

PP_i binding site. As mentioned above, both the $3D^{pol}$/GTP complex and the $3D^{pol}$/3′dUTP/VPg complex contain a PP_i bound to the central cavity where substrates are loaded, the reaction takes place, and the products are translocated or discarded. The PP_i is located between the NTP-binding motif F and motif E (Fig. 4A). While the P1 phosphate is strongly stabilized by interactions, interactions with the P2 phosphate group are weaker. The location of PP_i is identical in both structures. The data given below (distances and occupancies) relate to the higher-resolution complex $3D^{pol}$/PP_i(GTP).

Three basic residues from motif F (Arg163, Lys167, and Arg174) interact directly with one face of the PP_i. All three adopt two conformations, referred to as A and B, revealing the flexibility of motif-F side of the binding site. The A conformation of the side chain of Arg163 (70% occupancy) does not face the PP_i. The B conformation of the side chain of Arg163 points toward the oxygen atom O1 of P1. The distances between the NH1 and NH2 atoms, and the O1 atom (3.2 and 2.2 Å, respectively) are consistent with a salt bridge. The NH2 atom of Arg163 in the B conformation also interacts with the oxygen atom O3 of P1 (3.3 Å). Oxygen O6 of P2 may be stabilized by the NH1 atom (3.6 Å). The A conformation of Lys167 (50% occupancy) turns away from the PP_i. In the B conformation the NZ atom is positioned at 2.2 Å from the O6 atom of P2, allowing the formation of a salt bridge. Residue Arg174 in its A conformation (40% occupancy) interacts with O1 atom of P1 via its NH2 atom (2.4 Å). In the B conformation, Arg174 forms a salt bridge with the Glu161, as seen in the 1RA7 PV structure. We thus believe that the B conformations of Arg163 and Lys167 and the A conformation Arg174 correspond to the PP_i-bound form of CVB3 RdRp. On the other side, the PP_i group interacts with the side chains of two basic residues, Lys38 (index finger) and Lys376 (motif E). The NZ atom of the Lys38 is found at a distance of 2.8 Å from the O atom of the PP_i. The NZ atom of Lys376 may interact with the O2 atom of P1 (3.4 Å).

In summary, the observed PP_i near the active site is stabilized by several interactions with residues of motif F, the index finger, and motif E. It could represent either the β and γ phosphates of the NTP, a degradation product of these NTPs to NMP and PP_i, or an authentic PP_i product of the RdRp reaction. The latter possibility exists only in the case of the cocrystallization setup containing $3D^{pol}$, VPg, $oligoA_6$, 3′dUTP, and divalent ions, i.e., a complete RdRp initiation mix.

VPg binding site. The use of BUSTER-TNT 2.1.1 (3). made it possible to build the CVB3 VPg molecule and unambiguously position residues 7-PNQKPRVPT-15. This sequence was the consensus for the observed VPg peptide fragment after numerous independent modeling procedures. Several candi-

FIG. 4. Active-site cavity of CVB3 RdRp viewed toward the NTP tunnel entry with bound PP$_i$ in comparison to other RdRps complex structures. The PP$_i$ bound to CVB3 3D^{pol} is shown in sticks according to atom types in panel A and in green in panels B to E. (A) CVB3 RdRp NTP tunnel entry is partly closed by Lys61 and Lys360 seen in the background. A glycerol (behind PP$_i$) supports the contact to Lys167. PP$_i$, in sticks and colored according to atom type, is mainly contacted by motif F residues Arg174, Arg163, and Lys167 on the left and Lys38 and motif E residue Lys376 on the right. The motif F residues exist in double conformations, where conformations A, B, and B correspond to the PPi-binding forms of Arg174, Arg163, and Lys167, respectively. The left part of the cavity is filled by glycerol molecules. Catalytic residues are shown at the floor of the active-site cavity. (B) PV RdRp in complex with two manganese ions bound to catalytic residues and a GTP in site I (PDB ID:2ILZ). The side chains of residues, which shape the NTP entry tunnel and are decisive for PP$_i$ binding in CVB3 RdRp and conserved in PV RdRp, are shown in sticks. The NTP tunnel entry is partially closed by Lys359 contacted by Lys167 via a water molecule represented by a red sphere. Lys61 forms the left wall of a wider entry in comparison to CVB3 RdRp. (C) FMDV RdRp with a bound RNA primer/template after the reaction and translocation took place in the crystal (PDB ID:2EC0). The template is omitted, and only the two 3′-end nucleotides of the primer (CA) are shown. The PP$_i$ in site I (PP$_i$ in sticks colored according to the atom type) is thought to be the by-product of the reaction (14). The side chains of residues shaping the NTP entry tunnel and decisive for PP$_i$ binding in CVB3 RdRp, which are conserved in FMDV RdRp, are shown in sticks. (D) FMDV RdRp (PDB ID:2E9Z) with a bound primer/template after the reaction, a magnesium ion, and an UTP to be incorporated near site C. Again, the template is omitted, and only the two 3′-end nucleotides of the primer (CA) are shown. A PP$_i$ (PP$_i$ in sticks according to atom type) lies close to the CVB3 PPi. (E) Hepatitis C RdRp in complex with the triphosphate moiety (tP) of an NTP in a catalytic competent position at site C and two manganese ions (PDB ID:1GX5) and two triphosphates of NTPs at site P and site I (PDB ID:1GX6). Only the side chains of residues decisive for PP$_i$ binding in CVB3 RdRp and conserved in HCV RdRp are shown in sticks.

dates for the Pro7-Thr15 were modeled into the density. The best of these was chosen based on the lowest R values, best fit to 2 Fo-Fc density, cleanest Fo-Fc features, optimum bonding interactions with the protein, and best Ramachandran plot. The occupancy of all VPg atoms could be set to 1.0 during refinement without causing the associated B-factors to refine to abnormally high values, considering the high degree of exposure of VPg to solvent. However, we refined a group occupancy for all VPg atoms, which converged to a value of 0.9 with correspondingly lower B factors but essentially identical electron density maps. The difference between the two results has no impact on any conclusions we draw from the structure. Finally, we have kept VPg at an occupancy of 0.9 in the deposited structure. Figure 5A shows the 2|Fo|-|Fc| and |Fo|-|Fc| residual maps around VPg at the completion of the refinement. VPg binds to the base of the CVB3 3D^{pol} thumb subdomain (Fig. 3A and 5B). The binding site is located at the side and "back" of the polymerase at the transition zone between palm and thumb subdomains. As illustrated in Fig. 5B, VPg is far away from the "front" binding site observed in the FMDV RdRp/VPg-UMP complex (12). In contrast, the binding site we observe corresponds to the binding site identified earlier by mutational studies measuring VPg binding (in the context of membrane-bound 3AB) and uridylation by PV RdRp (34, 64). In that respect, our CVB3 RdRp/VPg structure confirms the existence of two VPg binding sites and reconciles previous VPg
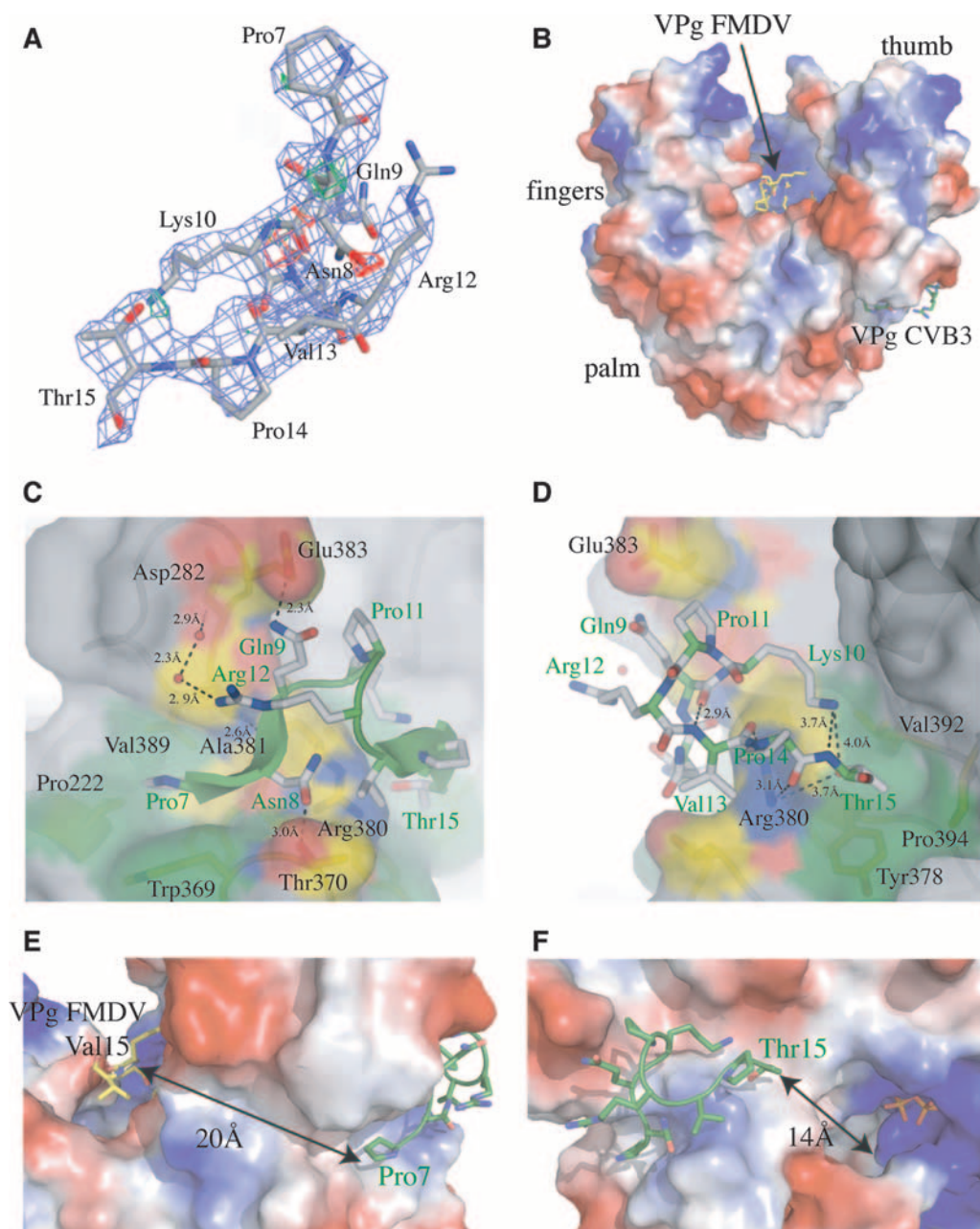
FIG. 5. CVB3 3D^{pol}-VPg complex. (A) Refined VPg model (in sticks, atoms colored according to atom types, C atoms in gray, N atoms in blue, and O atoms in red) with its 2Fo-Fc map (contoured at 0.8 sigma in blue) and its Fo-Fc map (in red = −3 sigma, in green = +3 sigma). (B) Electrostatic surface representation of CVB3 3D^{pol} (His$_6$ tag omitted) displaying positively charged (blue), negatively charged (red), and neutral (white) regions. VPg (in sticks colored according to atom types, C atoms in green) is bound to the base of the thumb domain, being far away from "front-loading" position near the active-site cavity where VPg was found in the FMDV RdRp-VPg complex (PDB ID:2F8E). FMDV VPg (in sticks colored according to atom types with C atoms in yellow) is shown after superimposing both complexes. (C) Close-up of CVB3 VPg shown in sticks and ribbon (short terminal β-strands). The C$_α$ atoms of the main chain of VPg are shown in green, the C atoms of the side chains in white, O atoms in red, and N atoms in blue. The residues of the VPg binding site of CVB3 3D^{pol} are shown in sticks colored according to the atom types (C in yellow, O in red, and N in blue). The surface of the hydrophobic pockets around Pro7 (Trp369, Pro222, and Val389) and Thr15 (Tyr378, Val392, and Pro394) is shown in green; the surface of the other residues is colored according to atom type. The interactions of Asp8, Gln9 and Arg12 are given in detail. Water molecules A677 and H274 are shown as red spheres. (D) Close-up on CVB3 VPg, which is shown in sticks. Coloring and representation of the VPg binding site of CVB3 3D^{pol} are as described for panel C. The internal interactions between Gln9 and Val13, as well as Lys10 and Thr15, are shown, as well as specific contacts of Pro14 and Thr15. (E) Illustration of the relative position of CVB3 VPg Pro7 to the front entrance of the RdRp, where superimposed FMDV VPg is seen, in particular Val15. Representation of the complex partners is maintained as in panel B. (F) Relative position of CVB3 VPg residue Thr15 toward the back entrance of the active-site cavity where the PP$_i$ is seen. The representation of complex partners is maintained as in panel B, PP$_i$ is shown in sticks and colored according to atom types.

binding site mapping studies with more recent structural data acquired on FMDV (12).

The VPg binding site of CVB3 3D^{Pol} comprises residues Trp369 and Thr370, motif-E β-strand-14 residues Tyr378 to Glu383, motif-E β-strand-15 residues Val389, Val392, and Pro394, as well as Pro222 from the palm subdomain (see Fig. 5C and D and Fig. 3). The VPg peptide has an α-helical turn at the center from Lys10 to Arg12 and extended β-strands at both ends, from Pro7 to Gln9 and from Val13 to Thr15 (Fig. 5C). It adopts the overall shape of an arch bridge that wraps around the CVB3 RdRp Arg380 side chain. Pro7 fits into a hydrophobic pocket lined by CVB3 RdRp residues Trp369, Pro222, and Val389 and stacks against the Trp369 side chain. The Asn8 side chain may hydrogen bond to the CVB3 RdRp Thr370 side chain (3.0 Å) and the Gln9 carbonyl group. The Asn8 carbonyl group β-sheet bonds to CVB3 RdRp Ala381 (2.6 Å). The Gln9 side chain hydrogen bonds to the CVB3 RdRp Glu383 side chain (2.3 Å) and stacks against the Arg12 guanidinium group and Pro11 on either side. The Gln9 carbonyl group hydrogen bonds internally to the main chain amide nitrogen of Val13 (2.9 Å), and this holds the alpha-helical turn (Fig. 5D). The VPg structure is further strengthened by weak hydrogen bonds between the Lys10 Nz atom and the side chain oxygen (4.0 Å) of Thr15 and/or main chain amide nitrogen (3.7 Å) of the same residue, the latter made possible at the high pH due to the possible lack of a positive charge of Lys10. The Arg12 side chain appears to be held in place by hydrogen bonding to the CVB3 RdRp Asp382 carbonyl group through two water molecules, as well as by the stacking interaction with the Gln9 side chain (Fig. 5C). The main chain carbonyl groups of VPg residues Val13 and Pro14 form hydrogen bonds to the CVB3 RdRp Arg380 side chain (3.1 Å for both, Fig. 5D). Finally, Thr15 fits into a pocket defined by the CVB3 RdRp Arg380, Tyr378, and Val392 side chains and Pro394, with the hydrophilic hydroxyl group pointing toward the Arg380 side chain (3.7 Å).

Figure 5E and F illustrate the spatial position and orientation of VPg in our complex in relation to the 3D^{Pol} active site. Essentially, Tyr3 seems too far away to serve as a primer for intramolecular uridylation. The distance between CVB3 VPg residue Pro7 and FMDV VPg Val15 from the superimposed front-loading FMDV RdRp/VPg complex is ~20 Å (Fig. 5E). Considering an extended conformation, the peptide stretch Tyr3 to Val6 would correspond to only 14.4 Å (3.6 Å per residue). The other possibility, which corresponds to a model proposed for PV RdRp/VPg (64), is that Tyr3 enters the active site from the back of the molecule. In this model VPg is oriented in the opposite sense compared to our complex structure where the residue closest to the back entry of the active site (NTP entry tunnel) is Thr15 (Fig. 5F).

In summary, the CVB3 3D^{Pol}/VPg complex structurally confirms the second VPg binding site at the base of the thumb subdomain, but the orientation of VPg at this site does not allow its uridylation by the same 3D^{Pol} molecule without dissociation and reassociation.

DISCUSSION

In the present study, we have determined the structure of an active (Fig. 1) CVB3 3D^{Pol} in complex with a PP$_i$ and its protein-primer VPg. The recombinant CVB3 RdRp elongated an oligo(dT)$_{15}$ primer on a poly(rA) template. Furthermore, it uridylated VPg using poly(rA) as a template. In our system we saw VPg uridylation exclusively when Mn^{2+} was used as catalytic ion (Fig. 1C). This corresponds to observations reported by others where VPg uridylation by PV and CVB3 RdRps in vitro needed to be activated either by Mn^{2+} or, when Mg^{2+} is used, by the presence of 3CD^{Pro} or 3C^{Pro} (4, 45–48, 54). Another product, migrating slower in Tris-Tricine PAGE, (Fig. 1C) might correspond to VPg-poly(U), 3D^{Pol}-pU(pU), or poly(A)-(pU)$_n$. The intra- and intermolecular uridylation of PV 3D^{Pol} has been shown previously (53). In contrast to that study, where 0.5 mM Mn^{2+} was used, in our system at 0.1 mM Mn^{2+} we do not see evidence of 3D^{Pol} uridylation in the absence of either the template or VPg. Interestingly, when we used 0.8 mM Mn^{2+} we saw the slower migrating product band even in the absence of VPg, although it was considerably stronger in its presence (data not shown). This background band could be due to 3D^{Pol} uridylation but also to a putative terminal transferase activity of CVB3 3D^{Pol}, which has been shown for PV 3D^{Pol} (4, 41). Given that the nature of the slow-migrating band is not the central point of the present study, we did not further analyze it. Nevertheless, even considering that VPg could be a strong activator of 3D^{Pol} uridylation and of a putative terminal transferase activity of CVB3 3D^{Pol}, the slower-migrating band might correspond at least in part to VPg-poly(U) and thus CVB3 3D^{Pol} seems to elongate the primer VPg-pU(pU) on poly(rA) in the presence of Mn^{2+}.

The three-dimensional structure of CVB3 3D^{Pol} adopts the canonical fold of a primer-dependent RdRp with an encircled active site, with a small thumb subdomain providing a wide and accessible active site able to accommodate a primer/template. It resembles closely the structure of 3D^{Pol} of PV, the *Enterovirus* prototype, and to a lesser extent other known *Picornaviridae* RdRp structures of HRV and FMDV. As observed for PV 3D^{Pol}, the N terminus of CVB3 3D^{Pol} is anchored to a zone near motif A of the active site. This had been proposed to assure the correct positioning of motif-A residue Asp238 and in that way the correct conformation of the active site in the palm subdomain (66). Nevertheless, the recent structure of PV 3CD^{Pro} has shown that the conformation of the active site, including Asp238 is preformed even when the N terminus is not in its final position (36). A similar scenario may be assumed for CVB3 3CD^{Pro} and 3D^{Pol}.

An interesting difference to PV 3D^{Pol} can be found in the NTP entry tunnel. Whereas Lys61 of PV 3D^{Pol} is forming the tunnel wall and engages in a salt bridge with Glu177, CVB3 3D^{Pol} Lys61 obstructs the entrance of the tunnel partially. This might be due to the high pH value of the protein solution (pH 9.0) and the mother liquor (pH ~10.0). Since the actual pH value should be near the pKa value of 10.5 of the side chain amino group of a free lysine, the positive charge of Lys61 may be suppressed under crystallization conditions and the salt bridge to Glu177 weakened. In the CVB3 3D^{Pol} structure a glycerol molecule occupies the position of side chain Lys61 in PV 3D^{Pol}. Lys61 was shown to be essential for activity of PV RdRp in vitro (52). Nevertheless, it is not involved in direct contacts with NTPs either in structures of PV RdRp (65) or in FMDV RdRp (14). Our activity tests showed that CVB3 RdRp was active at pH 8.0 and a low salt concentration, where Lys61

should bear a positive charge and might engage in the salt bridge with Glu177. The observed conformation of Lys61 side chain might thus be a consequence of the crystallization conditions.

A PP$_i$ was identified near the active site being engaged in a network of interactions with ring-finger motif F residues on one side, one residue from the index finger, and one from motif E between palm and thumb subdomains on the other side (Fig. 4A). In the cocrystallization mix, which contained only 3D^{pol}, GTP, and Mg^{2+}, the generation of PP$_i$ due to RdRp activity is unexpected. In the VPg cocrystallization mix all reaction partners are present (3D^{pol}, VPg, oligoA$_6$, 3'dUTP, and MgCl$_2$). Nevertheless, PP$_i$ generation by VPg-uridylation is unlikely, because the optimum pH used for VPg uridylation tests of CVB3 3D^{pol} is ~7.5 (65, 66), whereas the pH of the cocrystallization mix is considerably higher (between 9 and 10). We surmise that PP$_i$ is either generated by the degradation of NTP to NMP and PP$_i$ or is the sole visible part of an NTP, corresponding to the triphosphate moieties of various NTPs observed in HCV RdRp/NTP complexes (5).

How does the PP$_i$-binding site or putative NTP-binding site in CVB3 RdRp compare to known RdRp PP$_i$- or NTP-binding sites? For PV RdRp several complexes have been reported with all four NTPs binding to one site (Fig. 4B) (65, 66). This site is near the catalytic center, but the NTPs are not in a catalytically competent position since their triphosphates are not positioned over the aspartic acid residues of the active site. They overlap with the interrogation site (I) defined by complexes of bacteriophage φ6 and HCV RdRps (5, 7). In CVB3 RdRp the NTP-binding pocket is altered in comparison to PV RdRp. Part of the NTP-binding pocket is formed by the Lys61-Glu177 salt bridge, which does not exist in CVB3 RdRp as described above. The change of position of Lys61 creates a larger cavity that appears to be occupied by glycerol molecules (Fig. 4A). The PP$_i$ in CVB3 3D^{pol} is ~7 Å away from the PV 3D^{pol} NTP phosphates at site I (see Fig. 5B). Several ternary complexes of FMDV RdRp were recently reported (14). One (PDB ID:2EC0) contains a template/primer with an AMP having been incorporated into RNA within the crystal. The product has then been translocated, thus the AMP resides in the priming site (P). In addition, there is a PP$_i$ situated at site I (Fig. 4C), which was considered as a by-product of the RdRp reaction by the authors of that study. Another complex (PDB ID:2E9Z) contained the same reaction product, a new NTP substrate (UTP) in the catalytic site (C), as well as another PP$_i$ situated near the PP$_i$ found in CVB3 RdRp (Fig. 4D). Finally, de novo initializing HCV RdRp has been crystallized in complex with NTPs (5). In each case only the triphosphate moieties were visible and situated in a catalytic competent position in site C (PDB ID:1GX5) or in sites P and I (PDB ID:1GX6). The distances between these triphosphates and the PP$_i$ found in CVB3 3D^{pol} are ca. 8, 4, and 5 Å, respectively.

A comparison of these complexes and the PP$_i$ in CVB3 RdRp shows that it is closest to the PP$_i$ in the complex of FMDV RdRp shown in Fig. 4D. The closest distance between two phosphate atoms is 2.4 Å. Two hypotheses may be considered. First, our PP$_i$ represents the GTP or 3'dUTP, which thus would occupy a new, alternate NTP-binding site. The PP$_i$ might represent an NTP waiting to enter site I. This would support the proposal that the PP$_i$ in site I of the FMDV RdRp

FIG. 6. Alignment of *Picornaviridae* VPg peptides. CVB3 VPg (NCBI:gi:323421) is aligned to VPgs of PV (NCBI:NP740475) and of strains 14 (NCBI:P03303), 1B (NCBI:P12916), and 16 (NCBI:Q82122) of HRV and to the three VPgs of FMDV (NCBI:P03305). A thick bar above the alignment marks the VPg fragment visible in the CVB3 3D^{pol} complex. A thin bar marks residues that establish specific interactions to CVB3 3D^{pol} residues.

complex in Fig. 4C is the reaction by-product (14). Following this hypothesis, during the reaction, an NTP binds to site I, the interrogation takes place, it shifts to site C, a reaction takes place, the PP$_i$ moves back into I and is then discarded, a new NTP arrives from our site, which could be named "pre-I", and so on. The left part of the NTP tunnel (see Fig. 4) would then be the exit, the right part the entry and motif F would transfer the NTP from the pre-I to the I site. The second possibility is that our PP$_i$, generated by NTP degradation or RdRp activity, mimics a reaction product, and thus we see a genuine PP$_i$ binding site, which is very close to the second PP$_i$ binding site found in FMDV RdRp (14). This goes along with the scenario that site C could be occupied by an NTP, which is incorporated, whereas site I by another NTP, which waits for liberation of site C. The PP$_i$ of the first NTP has then to leave the active site via a different way than site I, and this could be via the PP$_i$-binding sites observed by Ferrer-Orta et al. (14) and us. Thus, the second hypothesis places the NTP entry on the left and the PP$_i$ exit on the right.

Finally, and most importantly, we were able to obtain a complex structure of CVB3 3D^{pol} with VPg, the latter interacting with CVB3 RdRp residues Pro222, Trp 369, Thr370, Tyr378 through to Glu383, Val390, Val392, and Pro394. This VPg binding site on CVB3 3D^{pol} includes residues corresponding to PV 3D^{pol} residues Phe377, Arg379, Glu382, and Val391 identified on PV RdRp as interacting residues in binding studies (26, 34, 64). Given the relatively high sequence and structural conservation between *Picornaviridae* RdRps and VPgs (Fig. 3 and 6), we thus found structural evidence for the existence of the VPg binding site at the base of the thumb subdomain of *Picornaviridae* RdRps. Interestingly, mutation of these residues affect VPg uridylation but not primed RNA synthesis (34). The conclusion was drawn that the binding site is directly involved in VPg uridylation. When PV Phe377 and Arg379 were mutated to study the effect on VPg uridylation (4), the latter was found to result in a greater reduction in uridylation. In our CVB3 complex structure, this is in agreement with the corresponding residue Arg380 having a more intimate contact with VPg under the "bridge" via main-chain hydrogen bonds to two VPg residues. CVB3 3D^{pol} residue Tyr378, by contrast, is only one of four residues forming the Thr15 binding site. Its mutation should therefore leave this site still partially functional, which was indeed the case (4).

We observe that CVB3 VPg residues Pro7, Asn8, Gln9, and Arg12 form specific side chain interactions, whereas Val13 and

Pro14 contribute with main chain interactions or by maintaining the main chain VPg in a conformation apt for interaction. Also, Lys10 seems to be important to maintain the internal structure of VPg. Thr15 is engaged in hydrophobic interactions with the pocket formed by the Tyr378 and Val392 side chains and Pro394. PV VPg and 3AB residues important for the interaction with $3D^{pol}$ have been identified in several studies, but the results remain controversial. A recent study defined a contiguous polymerase-binding sequence (13-VPTIR-17) on PV VPg (63), whereas other studies (46, 64) showed N-terminal residues as Tyr3, Leu6, Lys9, and Lys10 to be involved in binding. The CVB3 RdRp/VPg complex can confirm part of the results of these studies showing the importance of Gln9, Lys10, and Val13 to Thr15. In accordance with the complex structure, PV VPg residues Pro7, Lys9, Lys10, and Pro14 were shown to be essential for viral growth (46).

Although the VPg binding site on CVB3 $3D^{pol}$ corresponds well to the binding site at the base of the thumb subdomain identified on PV $3D^{pol}$, some pairwise interactions do not correspond to those identified by mutagenesis studies and the orientation of CVB3 VPg is opposite to the one of PV VPg in the corresponding model (64). As shown in Fig. 5E and F, it is not possible that Tyr 3 of CVB3 VPg bound in the observed position could be uridylated by its own carrier $3D^{pol}$ molecule without dissociation and reassociation. We see two hypotheses for the functional role of VPg at the binding site observed in the CVB3 $3D^{pol}$ complex: (i) VPg functions as a substrate of uridylation at this position and is uridylated by a second $3D^{pol}$ molecule or (ii) VPg plays a scaffolding role either by forming part of a VPg-$3D^{pol}$ unit incompetent for RNA synthesis but necessary to stabilize a neighboring functional VPg-$3D^{pol}$ unit where a VPg is placed at the "front-loading" position of $3D^{pol}$ as observed in the FMDV RdRp complex (12), or by stabilizing the VPg at the "front-loading" position of the same $3D^{pol}$ molecule, thus forming a VPg-$3D^{pol}$-VPg unit.

The first hypothesis, wherein a second $3D^{pol}$ molecule uridylates VPg bound to a "carrier" $3D^{pol}$, is supported by observations that PV $3D^{pol}$ in vitro and in vivo forms extensive oligomeric arrays (33) and that dimerization or oligomerization was necessary for primer-dependent RdRp activity in vitro (25). What could a productive dimer look like? According to our complex structure the interaction of two $3D^{pol}$ molecules should rather involve the back entry to the active site of the functional RdRp molecule. Tyr3 has to reach the active site, with Pro7 being kept at the observed position of the carrier RdRp molecule. The aspartic acid residues are too far away from the front of the molecule to allow the Tyr3 of the bound VPg access to the active site. The back entry allows easier access since the catalytic residues Asp233 and Asp329 are at a distance of around 7 and 12 Å, respectively, from Lys360 at the entry of the NTP tunnel. Furthermore, PV $3D^{pol}$ residues Asp358 and Lys359 at the entrance of the NTP tunnel have been shown to be important for VPg uridylation but not for RNA elongation (34). The symmetry mates of CVB3 RdRp in the crystal structure contact the central molecule very loosely and do not provide a model for intermolecular uridylation irrespective of the presence or absence of VPg. Symmetry mates of PV RdRp structures of either the apo-enzyme, complexes, or the RdRp in the context of 3CD (23, 36, 65, 66) do not provide any reasonable model either. We therefore tried to

generate a model by FTDock (18) using surface shape and charge complementarity as criteria, in conjunction with a 14-Å distance between VPg Pro7 on the carrier $3D^{pol}$ molecule and the active site residues of the functional $3D^{pol}$ molecule as a spatial restraint. The solutions exclusively used the back site of the functional $3D^{pol}$ (data not shown). In conclusion, a complex where VPg situated at the binding site observed in our complex structure is uridylated by another $3D^{pol}$ molecule seems to be possible. However, residue Tyr3 of VPg at the carrier $3D^{pol}$ has to enter the active site of the functional $3D^{pol}$ via the NTP tunnel at the back of the molecule, and this simultaneous entrance of VPg and UTP might cause steric problems.

The second hypothesis proposes that VPg at the binding site observed in our complex stabilizes the initiation complex. One possibility is that it stabilizes the complex in the context of an oligomeric array containing two functionally different units, a scaffold VPg-$3D^{pol}$ and another VPg-$3D^{pol}$ unit competent for initiation where VPg binds at the "front-loading" position as observed in the FMDV RdRp complex (12). Another possibility is that in the functional initiation complex one $3D^{pol}$ binds two VPgs, where VPg at the bottom of the thumb stabilizes another VPg at the "front-loading" position. It has been shown that in a minimalistic VPg uridylation complex one $3D^{pol}$ molecule binds to one template *cre*(2C) molecule and two molecules of activating $3CD^{pro}$ (44). The corresponding number of VPg molecules is not known. VPg at the site we observe in our complex might directly affect the binding or correct positioning of the VPg substrate molecule in the "front-loading" position or that of the RNA template. Note that the UMP bound covalently to residue Tyr3 of priming FMDV VPg in the complex with the RdRp in the absence of a second VPg (12) is not correctly positioned in the active site either as a product of the first uridylation step or as a primer for the second uridylation. The stabilizing VPg could influence the positioning of the substrate VPg via its C terminus being situated near the NTP tunnel entry. An argument against the last scenario is the fact that we did we not succeed to find another "stabilized" VPg bound at the priming position. The reason might be that we deal with dynamic complexes. Their formation might also depend on the presence of other components of the replication complex.

The question remains why the first six residues of VPg in the CVB3 RdRp complex remain flexible. Where could they be placed in a putative initiation complex? For the first scenario where we propose that two $3D^{pol}$ molecules might be necessary for VPg uridylation, the first six VPg residues should not interact strongly with the carrier $3D^{pol}$ but rather make a bridge to and interact with the uridylating $3D^{pol}$. For the other scenario either other partners in the replication complex interact and stabilize the N and C termini of the scaffold VPg or the second VPg, which binds to the "front-loading" site of the same $3D^{pol}$ molecule, stabilizes the missing residues. The structures of larger complexes are needed to give us further insight.

In summary, we report the structure of CVB3 $3D^{pol}$ in complex with a PP_i and the protein primer VPg. The PP_i could represent a new preinterrogation site for NTP substrates or a site for the PP_i coproduct leaving the active site. The $3D^{pol}$/VPg complex presents the first structural evidence of the bind-

ing site of the protein primer VPg at the base of the thumb subdomain of *Picornaviridae* polymerase 3D^{pol}. VPg at this position could either act as a substrate in an intermolecular uridylation complex or stabilize the VPg uridylation complex. The determination of the structure of the RdRp will facilitate the development of drugs against CVB3. CVB3 RNA was shown to persist in the heart beyond acute infection (30, 51). This persistence during chronic cardiac disease suggests that antiviral drugs might be useful in the clinic. Furthermore, regarding acute infections in neonates and infants, it was shown that the initial viral load correlates with disease severity (71). Thus, a therapeutic window exists that may also allow an effective treatment of acute illness by antiviral molecules.

ACKNOWLEDGMENTS

REFERENCES

1. **Appleby, T. C., H. Luecke, J. H. Shim, J. Z. Wu, I. W. Cheney, W. Zhong, L. Vogeley, Z. Hong, and N. Yao.** 2005. Crystal structure of complete rhinovirus RNA polymerase suggests front loading of protein primer. J. Virol. **79:**277–288.
2. **Barnard, D. L.** 2006. Current status of anti-picornavirus therapies. Curr. Pharm. Des. **12:**1379–1390.
3. **Blanc, E., P. Roversi, C. Vonrhein, C. Flensburg, S. M. Lea, and G. Bricogne.** 2004. Refinement of severely incomplete structures with maximum likelihood in BUSTER-TNT. Acta Crystallogr. D Biol. Crystallogr. **60:**2210–2221.
4. **Boerner, J. E., J. M. Lyle, S. Daijogo, B. L. Semler, S. C. Schultz, K. Kirkegaard, and O. C. Richards.** 2005. Allosteric effects of ligands and mutations on poliovirus RNA-dependent RNA polymerase. J. Virol. **79:**7803–7811.
5. **Bressanelli, S., L. Tomei, F. A. Rey, and R. De Francesco.** 2002. Structural analysis of the hepatitis C virus RNA polymerase in complex with ribonucleotides. J. Virol. **76:**3482–3492.
6. **Bruenn, J. A.** 2003. A structural and primary sequence comparison of the viral RNA-dependent RNA polymerases. Nucleic Acids Res. **31:**1821–1829.
7. **Butcher, S. J., J. M. Grimes, E. V. Makeyev, D. H. Bamford, and D. I. Stuart.** 2001. A mechanism for initiating RNA-dependent RNA polymerization. Nature **410:**235–240.
8. **Castro, C., E. Smidansky, K. R. Maksimchuk, J. J. Arnold, V. S. Korneeva, M. Gotte, W. Konigsberg, and C. E. Cameron.** 2007. Two proton transfers in the transition state for nucleotidyl transfer catalyzed by RNA- and DNA-dependent RNA and DNA polymerases. Proc. Natl. Acad. Sci. USA **104:**4267–4272.
9. **Crawford, N. M., and D. Baltimore.** 1983. Genome-linked protein VPg of poliovirus is present as free VPg and VPg-pUpU in poliovirus-infected cells. Proc. Natl. Acad. Sci. USA **80:**7452–7455.
10. **Doublie, S., M. R. Sawaya, and T. Ellenberger.** 1999. An open and closed case for all polymerases. Structure **7:**R31–R35.
11. **Emsley, P., and K. Cowtan.** 2004. Coot: model-building tools for molecular graphics. Acta Crystallogr. D Biol. Crystallogr. **60:**2126–2132.
12. **Ferrer-Orta, C., A. Arias, R. Agudo, R. Perez-Luque, C. Escarmis, E. Domingo, and N. Verdaguer.** 2006. The structure of a protein primer-polymerase complex in the initiation of genome replication. EMBO J. **25:**880–888.
13. **Ferrer-Orta, C., A. Arias, C. Escarmis, and N. Verdaguer.** 2006. A comparison of viral RNA-dependent RNA polymerases. Curr. Opin. Struct. Biol. **16:**27–34.
14. **Ferrer-Orta, C., A. Arias, R. Perez-Luque, C. Escarmis, E. Domingo, and N. Verdaguer.** 2007. Sequential structures provide insights into the fidelity of RNA replication. Proc. Natl. Acad. Sci. USA **104:**9463–9468.
15. **Ferrer-Orta, C., A. Arias, R. Perez-Luque, C. Escarmis, E. Domingo, and N. Verdaguer.** 2004. Structure of foot-and-mouth disease virus RNA-dependent RNA polymerase and its complex with a template-primer RNA. J. Biol. Chem. **279:**47212–47221.
16. **Fujita, K., S. S. Krishnakumar, D. Franco, A. V. Paul, E. London, and E. Wimmer.** 2007. Membrane topography of the hydrophobic anchor sequence of poliovirus 3A and 3AB proteins and the functional effect of 3A/3AB membrane association upon RNA replication. Biochemistry **46:**5185–5199.
17. **Fullerton, S. W., M. Blaschke, B. Coutard, J. Gebhardt, A. Gorbalenya, B. Canard, P. A. Tucker, and J. Rohayem.** 2007. Structural and functional characterization of sapovirus RNA-dependent RNA polymerase. J. Virol. **81:**1858–1871.
18. **Gabb, H. A., R. M. Jackson, and M. J. Sternberg.** 1997. Modelling protein docking using shape complementarity, electrostatics, and biochemical information. J. Mol. Biol. **272:**106–120.
19. **Gauntt, C., and S. Huber.** 2003. Coxsackievirus experimental heart diseases. Front. Biosci. **8:**e23–e35.
20. **Goodfellow, I. G., C. Polacek, R. Andino, and D. J. Evans.** 2003. The poliovirus 2C *cis*-acting replication element-mediated uridylylation of VPg is not required for synthesis of negative-sense genomes. J. Gen. Virol. **84:**2359–2363.
21. **Gorbalenya, A. E., F. M. Pringle, J. L. Zeddam, B. T. Luke, C. E. Cameron, J. Kalmakoff, T. N. Hanzlik, K. H. Gordon, and V. K. Ward.** 2002. The palm subdomain-based active site is internally permuted in viral RNA-dependent RNA polymerases of an ancient lineage. J. Mol. Biol. **324:**47–62.
22. **Gouet, P., X. Robert, and E. Courcelle.** 2003. ESPript/ENDscript: extracting and rendering sequence and 3D information from atomic structures of proteins. Nucleic Acids Res. **31:**3320–3323.
23. **Hansen, J. L., A. M. Long, and S. C. Schultz.** 1997. Structure of the RNA-dependent RNA polymerase of poliovirus. Structure **5:**1109–1122.
24. **Herold, J., and R. Andino.** 2000. Poliovirus requires a precise 5′ end for efficient positive-strand RNA synthesis. J. Virol. **74:**6394–6400.
25. **Hobson, S. D., E. S. Rosenblum, O. C. Richards, K. Richmond, K. Kirkegaard, and S. C. Schultz.** 2001. Oligomeric structures of poliovirus polymerase are important for function. EMBO J. **20:**1153–1163.
26. **Hope, D. A., S. E. Diamond, and K. Kirkegaard.** 1997. Genetic dissection of interaction between poliovirus 3D polymerase and viral protein 3AB. J. Virol. **71:**9490–9498.
27. **Jabafi, I., B. Selisko, B. Coutard, A. M. De Palma, J. Neyts, M. P. Egloff, S. Grisel, K. Dalle, V. Campanacci, S. Spinelli, C. Cambillau, B. Canard, and A. Gruez.** 2007. Improved crystallization of the coxsackievirus B3 RNA-dependent RNA polymerase. Acta Crystallogr. Sect. F Struct. Biol. Crystallogr. Commun. **63:**495–498.
28. **Kabsch.** 1988. Evaluation of single-crystal X-ray diffraction data from a position-sensitive detector. J. Appl. Crystallogr. **21:**916–924.
29. **Krissinel, E., and K. Henrick.** 2004. Secondary-structure matching (SSM), a new tool for fast protein structure alignment in three dimensions. Acta Crystallogr. D Biol. Crystallogr. **60:**2256–2268.
30. **Li, Y., T. Bourlet, L. Andreoletti, J. F. Mosnier, T. Peng, Y. Yang, L. C. Archard, B. Pozzetto, and H. Zhang.** 2000. Enteroviral capsid protein VP1 is present in myocardial tissues from some patients with myocarditis or dilated cardiomyopathy. Circulation **101:**231–234.
31. **Liu, Y., D. Franco, A. V. Paul, and E. Wimmer.** 2007. Tyrosine 3 of poliovirus terminal peptide VPg(3B) has an essential function in RNA replication in the context of its precursor protein, 3AB. J. Virol. **81:**5669–5684.
32. **Love, R. A., K. A. Maegley, X. Yu, R. A. Ferre, L. K. Lingardo, W. Diehl, H. E. Parge, P. S. Dragovich, and S. A. Fuhrman.** 2004. The crystal structure of the RNA-dependent RNA polymerase from human rhinovirus: a dual function target for common antiviral therapy. Structure **12:**1533–1544.
33. **Lyle, J. M., E. Bullitt, K. Bienz, and K. Kirkegaard.** 2002. Visualization and functional analysis of RNA-dependent RNA polymerase lattices. Science **296:**2218–2222.
34. **Lyle, J. M., A. Clewell, K. Richmond, O. C. Richards, D. A. Hope, S. C. Schultz, and K. Kirkegaard.** 2002. Similar structural basis for membrane localization and protein priming by an RNA-dependent RNA polymerase. J. Biol. Chem. **277:**16324–16331.
35. **Malet, H., M. P. Egloff, B. Selisko, R. E. Butcher, P. J. Wright, M. Roberts, A. Gruez, G. Sulzenbacher, C. Vonrhein, G. Bricogne, J. M. Mackenzie, A. A. Khromykh, A. D. Davidson, and B. Canard.** 2007. Crystal structure of the RNA polymerase domain of the West Nile virus nonstructural protein 5. J. Biol. Chem. **282:**10678–10689.
36. **Marcotte, L. L., A. B. Wass, D. W. Gohara, H. B. Pathak, J. J. Arnold, D. J. Filman, C. E. Cameron, and J. M. Hogle.** 2007. Crystal structure of poliovirus 3CD protein: virally encoded protease and precursor to the RNA-dependent RNA polymerase. J. Virol. **81:**3583–3596.
37. **Morasco, B. J., N. Sharma, J. Parilla, and J. B. Flanegan.** 2003. Poliovirus cre(2C)-dependent synthesis of VPgpUpU is required for positive- but not negative-strand RNA synthesis. J. Virol. **77:**5136–5144.
38. **Murray, K. E., and D. J. Barton.** 2003. Poliovirus CRE-dependent VPg

uridylylation is required for positive-strand RNA synthesis but not for neg-
ative-strand RNA synthesis. J. Virol. **77:**4739–4750.

39. **Murshudov, G. N., A. A. Vagin, and E. J. Dodson.** 1997. Refinement of
    macromolecular structures by the maximum-likelihood method. Acta Crys-
    tallogr. D Biol. Crystallogr. **53:**240–255.

40. **Navaza, J.** 2001. Implementation of molecular replacement in AMoRe. Acta
    Crystallogr. D Biol. Crystallogr. **57:**1367–1372.

41. **Neufeld, K. L., J. M. Galarza, O. C. Richards, D. F. Summers, and E.
    Ehrenfeld.** 1994. Identification of terminal adenylyl transferase activity of the
    poliovirus polymerase 3Dpol. J. Virol. **68:**5811–5818.

42. **Ng, K. K., M. M. Cherney, A. L. Vazquez, A. Machin, J. M. Alonso, F. Parra,
    and M. N. James.** 2002. Crystal structures of active and inactive conforma-
    tions of a caliciviral RNA-dependent RNA polymerase. J. Biol. Chem. **277:**
    1381–1387.

43. **Pan, J., V. N. Vakharia, and Y. J. Tao.** 2007. The structure of a birnavirus
    polymerase reveals a distinct active site topology. Proc. Natl. Acad. Sci. USA
    104:7385–7390.

44. **Pathak, H. B., J. J. Arnold, P. N. Wiegand, M. R. Hargittai, and C. E.
    Cameron.** 2007. Picornavirus genome replication: assembly and organization
    of the VPg uridylylation ribonucleoprotein (initiation) complex. J. Biol.
    Chem. **282:**16202–16213.

45. **Pathak, H. B., S. K. Ghosh, A. W. Roberts, S. D. Sharma, J. D. Yoder, J. J.
    Arnold, D. W. Gohara, D. J. Barton, A. V. Paul, and C. E. Cameron.** 2002.
    Structure-function relationships of the RNA-dependent RNA polymerase
    from poliovirus (3Dpol): a surface of the primary oligomerization domain
    functions in capsid precursor processing and VPg uridylylation. J. Biol.
    Chem. **277:**31551–31562.

46. **Paul, A. V., J. Peters, J. Mugavero, J. Yin, J. H. van Boom, and E. Wimmer.**
    2003. Biochemical and genetic studies of the VPg uridylylation reaction
    catalyzed by the RNA polymerase of poliovirus. J. Virol. **77:**891–904.

47. **Paul, A. V., E. Rieder, D. W. Kim, J. H. van Boom, and E. Wimmer.** 2000.
    Identification of an RNA hairpin in poliovirus RNA that serves as the
    primary template in the in vitro uridylylation of VPg. J. Virol. **74:**10359–
    10370.

48. **Paul, A. V., J. H. van Boom, D. Filippov, and E. Wimmer.** 1998. Protein-
    primed RNA synthesis by purified poliovirus RNA polymerase. Nature **393:**
    280–284.

49. **Perrakis, A., R. Morris, and V. S. Lamzin.** 1999. Automated protein model
    building combined with iterative structure refinement. Nat. Struct. Biol.
    6:458–463.

50. **Racaniello, V. R.** 2001. Picornaviridae: the viruses and their replication, p.
    685–722. *In* D. M. Knipe and P. M. Howley (ed.), Fields' virology, 4th ed.,
    vol. 1. Lippincott/The Williams & Wilkins Co., Philadelphia, PA.

51. **Reetoo, K. N., S. A. Osman, S. J. Illavia, C. L. Cameron-Wilson, J. E.
    Banatvala, and P. Muir.** 2000. Quantitative analysis of viral RNA kinetics in
    coxsackievirus B3-induced murine myocarditis: biphasic pattern of clearance
    following acute infection, with persistence of residual viral RNA throughout
    and beyond the inflammatory phase of disease. J. Gen. Virol. **81:**2755–2762.

52. **Richards, O. C., S. Baker, and E. Ehrenfeld.** 1996. Mutation of lysine resi-
    dues in the nucleotide binding segments of the poliovirus RNA-dependent
    RNA polymerase. J. Virol. **70:**8564–8570.

53. **Richards, O. C., J. F. Spagnolo, J. M. Lyle, S. E. Vleck, R. D. Kuchta, and
    K. Kirkegaard.** 2006. Intramolecular and intermolecular uridylylation by
    poliovirus RNA-dependent RNA polymerase. J. Virol. **80:**7405–7415.

54. **Rieder, E., A. V. Paul, D. W. Kim, J. H. van Boom, and E. Wimmer.** 2000.

55. **Rohayem, J., K. Jager, I. Robel, U. Scheffler, A. Temme, and W. Rudolph.**
    2006. Characterization of norovirus 3D^{pol} RNA-dependent RNA polymer-
    ase activity and initiation of RNA synthesis. J. Gen. Virol. **87:**2621–2630.

56. **Rohayem, J., I. Robel, K. Jager, U. Scheffler, and W. Rudolph.** 2006. Protein-
    primed and de novo initiation of RNA synthesis by norovirus 3D^{pol}. J. Virol.
    80:7060–7069.

57. **Roussel, A., and C. Cambillau.** 1991. Turbo-Frodo: Silicon Graphics geom-
    etry partners directory. Silicon Graphics, Mountain View, CA.

58. **Schein, C. H., N. Oezguen, D. E. Volk, R. Garimella, A. Paul, and W. Braun.**
    2006. NMR structure of the viral peptide linked to the genome (VPg) of
    poliovirus. Peptides **27:**1676–1684.

59. **Sean, P., and B. L. Semler.** 2008. Coxsackievirus B RNA replication: lessons
    from poliovirus. Curr. Top. Microbiol. Immunol. **323:**89–121.

60. **Senior, K.** 2002. FDA panel rejects common cold treatment. Lancet Infect.
    Dis. **2:**264.

61. **Smart, O. S., M. Brandl, C. Flensburg, P. Keller, W. Paciorek, C. Vonrhein,
    T. O. Womack, and G. Bricogne.** 2008. Refinement with local structure
    similarity restraints (LSSR) enables exploitation of information from related
    structures and facilitates use of NCS, abstr. TP139. Abstr. Annu. Meet. Am.
    Crystallogr. Assoc., Knoxville, TN.

62. **Steitz, T. A.** 1998. A mechanism for all polymerases. Nature **391:**231–232.

63. **Strauss, D. M., and D. S. Wuttke.** 2007. Characterization of protein-protein
    interactions critical for poliovirus replication: analysis of 3AB and VPg
    binding to the RNA-dependent RNA polymerase. J. Virol. **81:**6369–6378.

64. **Tellez, A. B., S. Crowder, J. F. Spagnolo, A. A. Thompson, O. B. Peersen,
    D. L. Brutlag, and K. Kirkegaard.** 2006. Nucleotide channel of RNA-de-
    pendent RNA polymerase used for intermolecular uridylylation of protein
    primer. J. Mol. Biol. **357:**665–675.

65. **Thompson, A. A., R. A. Albertini, and O. B. Peersen.** 2007. Stabilization of
    poliovirus polymerase by NTP binding and fingers-thumb interactions. J.
    Mol. Biol. **366:**1459–1474.

66. **Thompson, A. A., and O. B. Peersen.** 2004. Structural basis for proteolysis-
    dependent activation of the poliovirus RNA-dependent RNA polymerase.
    EMBO J. **23:**3462–3471.

67. **van Ooij, M. J., D. A. Vogt, A. Paul, C. Castro, J. Kuijpers, F. J. van
    Kuppeveld, C. E. Cameron, E. Wimmer, R. Andino, and W. J. Melchers.**
    2006. Structural and functional characterization of the coxsackievirus B3
    CRE(2C): role of CRE(2C) in negative- and positive-strand RNA synthesis.
    J. Gen. Virol. **87:**103–113.

68. **Whitton, J. L., C. T. Cornell, and R. Feuer.** 2005. Host and virus determi-
    nants of picornavirus pathogenesis and tropism. Nat. Rev. Microbiol. **3:**765–
    776.

69. **Yang, Y., R. Rijnbrand, S. Watowich, and S. M. Lemon.** 2004. Genetic
    evidence for an interaction between a picornaviral *cis*-acting RNA replica-
    tion element and 3CD protein. J. Biol. Chem. **279:**12659–12667.

70. **Yap, T. L., T. Xu, Y. L. Chen, H. Malet, M. P. Egloff, B. Canard, S. G.
    Vasudevan, and J. Lescar.** 2007. Crystal structure of the dengue virus RNA-
    dependent RNA polymerase catalytic domain at 1.85-Å resolution. J. Virol.
    81:4753–4765.

71. **Yen, M. H., K. C. Tsao, Y. C. Huang, C. G. Huang, Y. L. Huang, R. Lin, M. L.
    Chang, C. C. Huang, D. C. Yan, and T. Y. Lin.** 2007. Viral load in blood is
    correlated with disease severity of neonatal coxsackievirus B3 infection: early
    diagnosis and predicting disease severity is possible in severe neonatal en-
    terovirus infection. Clin. Infect. Dis. **44:**e78–e81.

Genetic and biochemical studies of poliovirus *cis*-acting replication element
cre in relation to VPg uridylylation. J. Virol. **74:**10371–10380.